

Article

# Patch-Based Local Climate Zones Mapping and Population Distribution Pattern in Provincial Capital Cities of China

Liang Zhou <sup>1</sup>, Lei Ma <sup>1,\*</sup>, Brian Alan Johnson <sup>2</sup>, Ziyun Yan <sup>1</sup>, Feixue Li <sup>1</sup> and Manchun Li <sup>1</sup>

- <sup>1</sup> Jiangsu Provincial Key Laboratory of Geographic Information Science and Technology, Key Laboratory for Land Satellite Remote Sensing Applications of Ministry of Natural Resources, School of Geography and Ocean Science, Nanjing University, Nanjing 210023, China; mg20270122@smail.nju.edu.cn (L.Z.); mg21270109@smail.nju.edu.cn (Z.Y.); lifeixue@nju.edu.cn (F.L.); limanchun@nju.edu.cn (M.L.)  
<sup>2</sup> Natural Resources and Ecosystem Services, Institute for Global Environmental Strategies, 2108-11, Kamiyamaguchi, Hayama, Kanagawa 240-0115, Japan; johnson@iges.or.jp  
 \* Correspondence: malenju@nju.edu.cn

**Abstract:** Accurate urban morphology provided by Local Climate Zones (LCZ), a universal surface classification scheme, offers opportunities for studies of urban heat risk, urban ventilation, and transport planning. In recent years, researchers have attempted to generate LCZ maps worldwide with the World Urban Database and Access Portal Tools (WUDAPT). However, the accuracy of LCZ mapping is not satisfactory and cannot fulfill the quality demands of practical usage. Here, we constructed a high-quality sample dataset from Chinese cities and presented a patch-based classification framework that employs chessboard segmentation and multi-seasonal images for LCZ mapping. Compared with the latest WUDAPT method, the overall accuracy for all LCZ types (OA) and urban LCZ types (OA<sub>u</sub>) of our framework increased by about 10% and 9%, respectively. Furthermore, based on the analysis of population distribution, we first gave the population density of different built-up LCZs of Chinese cities and found a hierarchical effect of population density among built-up LCZs in different size cities. In summary, this study could serve as a valuable reference for producing high-quality LCZ maps and understanding population distribution patterns in built-up LCZ types.

**Keywords:** local climate zones; patch-based classification; multi-seasonal images; WUDAPT; population distribution pattern; Chinese cities

**Citation:** Zhou, L.; Ma, L.; Johnson, B.A.; Yan, Z.; Li, F.; Li, M. Patch-Based Local Climate Zones Mapping and Population Distribution Pattern in Provincial Capital Cities of China. *ISPRS Int. J. Geo-Inf.* **2022**, *11*, 420. <https://doi.org/10.3390/ijgi11080420>

Academic Editors: Mingshu Wang and Wolfgang Kainz

Received: 18 May 2022  
 Accepted: 7 July 2022  
 Published: 25 July 2022

**Publisher's Note:** MDPI stays neutral with regard to jurisdictional claims in published maps and institutional affiliations.



**Copyright:** © 2022 by the authors. Licensee MDPI, Basel, Switzerland. This article is an open access article distributed under the terms and conditions of the Creative Commons Attribution (CC BY) license (<https://creativecommons.org/licenses/by/4.0/>).

## 1. Introduction

In recent decades, the world has experienced an unprecedented process of urbanization. According to the latest report of the United Nations Habitat (UNH), although urban areas account for only 3% of the world's land area, 55% of the population lives in urban areas; this number is expected to increase to 68% by 2050 [1]. Rapid and unplanned urbanization, coupled with the challenges brought by climate change, can lead to environmental and health problems [2,3] in many cities, thereby affecting the sustainable development of cities. The lack of globally consistent data on cities makes it difficult to understand the overall impact of urbanization. However, remote sensing technology provides a source of data for this challenge; especially, the Landsat-8 satellite of the National Aeronautics and Space Administration (NASA) and the Sentinel-2 satellite of the European Space Agency (ESA) provide continuous, reliable, and quality-controlled earth observation data that are free and open.

Through remote sensing data and artificial intelligence techniques, some scholars have generated several datasets on the extent of global urban boundaries, such as Global Urban Footprint (GUF) [4], Global Human Settlement Layer (GHSL) [5], and Global Artificial Impervious Area (GAIA) [6], which provide a binary mask of urban and non-

urban surfaces. In addition, there are some land use/land cover (LULC) datasets, such as the global land cover map (GLC) [7,8] and ESA Climate Change Initiative Land Cover (CCI-LC) [9], which represent urban areas through impervious surfaces. Through these global urban boundary datasets and LULC datasets, the growth and rate of global urbanization can be monitored at the city scale. However, many international efforts to address the issues of urbanization, such as the United Nation's call for "Sustainable Cities and Communities", are based on accurate measurements of urban morphological and demographic figures that can provide key scientific foundations for allocating valuable resources for a wide range of stakeholders [10]. These binary urban masks and LULC datasets cannot provide sufficient spatial details to describe cities' internal structures and functions.

To address this issue, Stewart and Oke [11] proposed a Local Climate Zone (LCZ) classification system, which is composed of ten built-up, or artificial, LULC types (LCZs 1–10; Figure 1) and seven natural LULC types (LCZs A-G; Figure 1). The LCZ types are defined as areas with uniform surface cover, structure, material, and human activity, spanning hundreds of meters to several kilometers on the horizontal scale [11]. Since the LCZ scheme was originally designed for standardizing the exchange of urban temperature observations, urban heat island studies under the LCZ classification scheme have been conducted in more than 130 cities worldwide in recent years [12]. At the same time, the LCZ scheme also provides a numerical description of urban canopy parameters that are rare in traditional LULC classification but are key in the urban ecosystem. This has made LCZ data attractive for a wide range of applications, including urban planning [13,14], urban energy demand modeling [15,16], urban ventilation simulation [17–19], and outdoor thermal comfort monitoring [20,21].

The LCZ classification scheme was originally designed for urban climatic studies [11,22], and the reference population range for each LCZ type was not given [23]. However, LCZ maps can also be used to better understand the urban population distribution, as the built-up LCZs have relatively distinct traits in building size, height, density, and usage. Demuzere et al. [23] found the population data in the LCZs agreed with their classification when they mapped the continental United States into LCZ types. In addition, Hu et al. [24] combined LCZ maps with population density to analyze urban land consumption at an intra-urban spatial scale over 40 cities worldwide. However, few studies have examined the relationship between LCZs and population data on a national scale, especially in China, the world's most populous country. Furthermore, it is unknown how different city sizes affect population distribution in LCZs.

There are many methods for generating LCZ maps, including traditional sampling through field surveys, geographic information system (GIS) approaches, and remote sensing image classification approaches [25–30]. Classification based on remote sensing images provides a fast and economical method for LCZ mapping and has been widely used in prior studies [31–36]. Bechtel et al. [26] designed a pixel-based supervised classification approach, which uses Landsat-8 images and the random forest classification algorithm [37], to generate an LCZ map with a resolution of 100 m. The method was used by the World Urban Database and Access Portal Tools (WUDAPT) project to create a database for uploading LCZ samples and then generated LCZ maps of different cities around the world [38]. Demuzere et al. [39] then designed an online platform (LCZ-Generator) to simplify the default WUDAPT classification workflow further. Only 150 cities worldwide have had their LCZ map and corresponding samples uploaded to the WUDAPT website [39], and these maps may be quickly outdated due to rapid LULC changes occurring in/around urban areas. Although more and more training area sets have been submitted to the LCZ Generator recently, the samples from different cities cannot be consistent. Currently, only Europe [40] and the continental United States [23] have a complete LCZ map. Thus, there is a need for a high-quality training sample set with label information to generate a complete LCZ map of China.

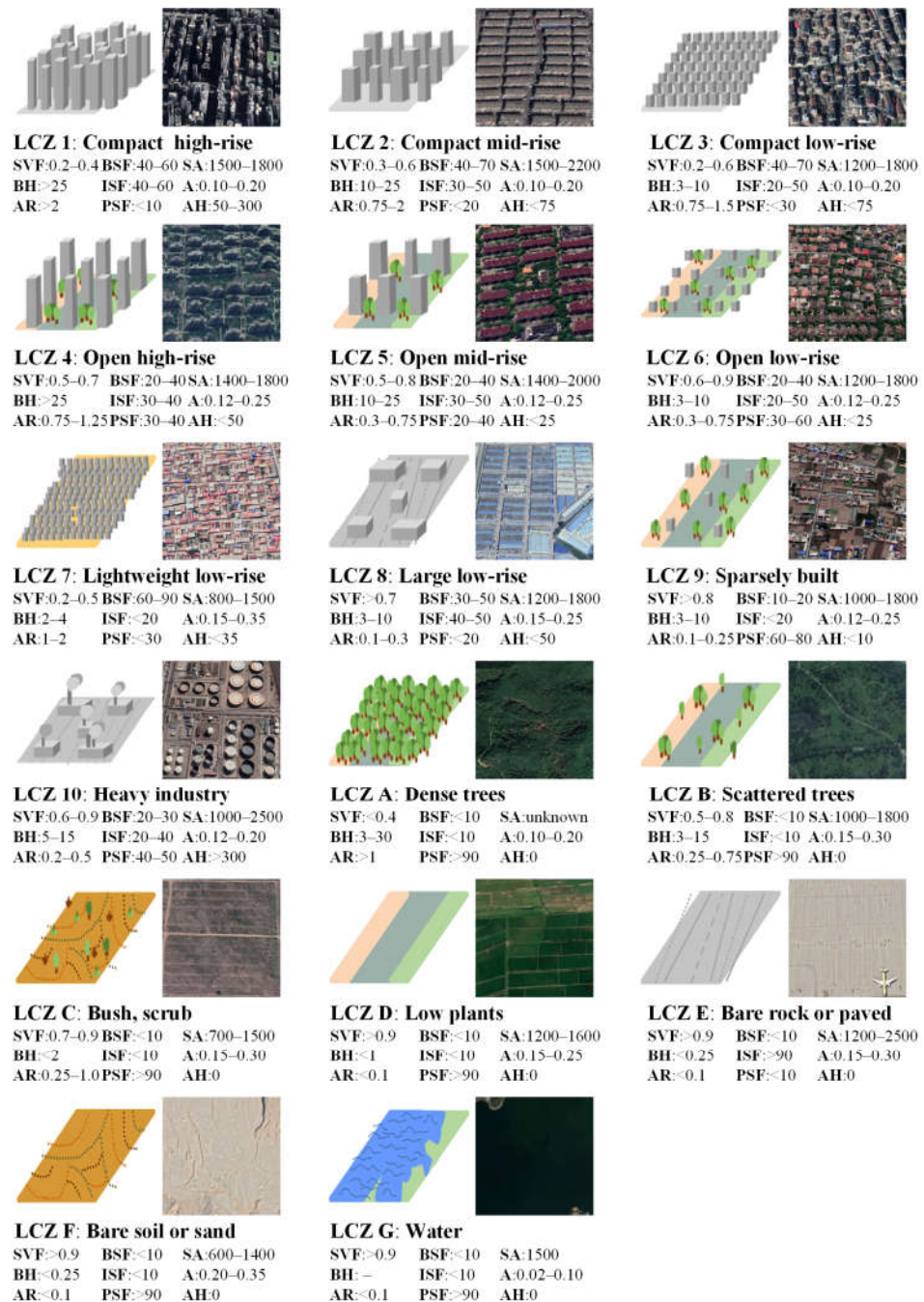


**Figure 1.** Classification of local climate zones and range of urban canopy parameters based on [11]. (Note: The top-left corner of each LCZ type is the schematic drawings given by [41]. The top-right corner of each LCZ type is the representative high-resolution images from Google Earth. SVF means sky view factor; BSF means building surface fraction; SA means surface admittance; BH means height of roughness elements; ISF means impervious surface fraction; A means surface albedo; AR means aspect ratio; PSF means pervious surface fraction; AH means anthropogenic heat.).

Different quality evaluation results show that the accuracy of LCZ mapping obtained by the WUDPAT method is often not high [41,42]. The WUDAPT method is pixel based, which relies heavily on spectral information of image pixels, i.e., electromagnetic reflectance at different wavelengths. However, due to the differences in cultural and physical environmental factors (e.g., construction materials and vegetation types), LCZ

types in different cities often have different spectral characteristics. Therefore, LCZ classification approaches based only on spectral information of pixels alone cannot achieve high accuracy. Remote sensing researchers have found that texture information is helpful for image classification tasks [43], particularly when image pixels are smaller than the LULC features of interest (as individual pixels represent only a portion of the feature of interest in this case). Patch-based classification approaches can better take advantage of contextual information provided by neighboring pixels, e.g., local spectral heterogeneity. Some scholars have put forward deep learning methods such as CNN and FCN [35,36,44], which also incorporate patch-based features, or utilized auxiliary data such as building height data [32,45] to improve LCZ mapping accuracy. However, because of limitations in the training data or image data available in most cities, these methods are not universal at present. At the same time, the classification results vary significantly with the spatial scale at which LCZ maps are produced [26,41]. Stewart and Oke [11] suggested that the minimum radius of each LCZ should be between 200–500m. Liu et al. [44] used Sentinel-2 imagery with a 10 m spatial resolution for LCZ mapping and found that the optimal image sizes were from 32 to 64. Zheng et al. [28] conducted LCZ mapping in Hong Kong and found that the optimal mapping scale was 300 m. Aside from the use of contextual information from neighboring pixels, many studies have shown that multi-seasonal information from remote sensing imagery can help optimize the mapping results of land cover classification [46,47] and significantly improve the cartographic accuracy of LCZ classification [36,48,49]. Based on the above information from previous works, it is evident that the 300 m resolution, multi-temporal and patch-based LCZ classification framework could be successful for LCZ mapping across multiple cities.

This study aimed to: (1) construct a high-quality training sample set with label information in 34 provincial capital cities of China, (2) propose a classification framework to improve LCZ mapping accuracy, (3) study population distribution in LCZs on a national scale, and (4) further explore how different city sizes affect population distribution in LCZs. To achieve these objectives, we outlined and labeled sample polygons using high-resolution images from Google Earth. Then, we proposed an LCZ classification framework based on chessboard segmentation and multi-seasonal Sentinel-2 images on a 300 m grid and used this framework to generate LCZ maps in 34 provincial capital cities of China. Then, an overlay analysis was performed to analyze the relation between LCZ classification results with the population data on a national scale. Finally, the influence of city size on population distribution in LCZ was analyzed by classifying cities based on the number of urban permanent populations.

## 2. Materials and Methods

### 2.1. Study Area

China is a vast and populous country located in the east of Asia and on the west coast of the Pacific Ocean (73°33'–135°05' E; 3°51'–53°33' N), as shown in Figure 2. Due to the huge differences in geographical conditions, China's climate is complex and diverse. Climatic types include tropical climates in the south to cold temperate climates in the north and plateau mountain climates in the Qinghai-Tibet Plateau. The southeastern part of China is densely populated, and the northwestern part is sparsely populated. The diversity of climate and the uneven distribution of population lead to huge differences in urban landscapes in China.

Chinese cities were classified according to the new city size classification standard issued by China [50] and were divided into four sizes according to the urban permanent residents in the study area (Table S1). In the analysis of Section 3.3, we excluded Macao and Lasa because these two cities differ greatly in urban form apart from the similarities in terms of population. Meanwhile, the number of medium-sized cities is too small for the results to be representative.

In this study, we conducted LCZ mapping and population distribution analysis in 34 major Chinese cities. These 34 cities represent municipalities or provincial capitals located in different climatic zones and contain a variety of complex urban forms and landscapes. The extent of the study area of each city considered for our analysis was determined by the GUB dataset and the city's administrative boundary to reduce the non-urban areas significantly. We show the boundary derived for Wuhan in Figure 2 as an example.

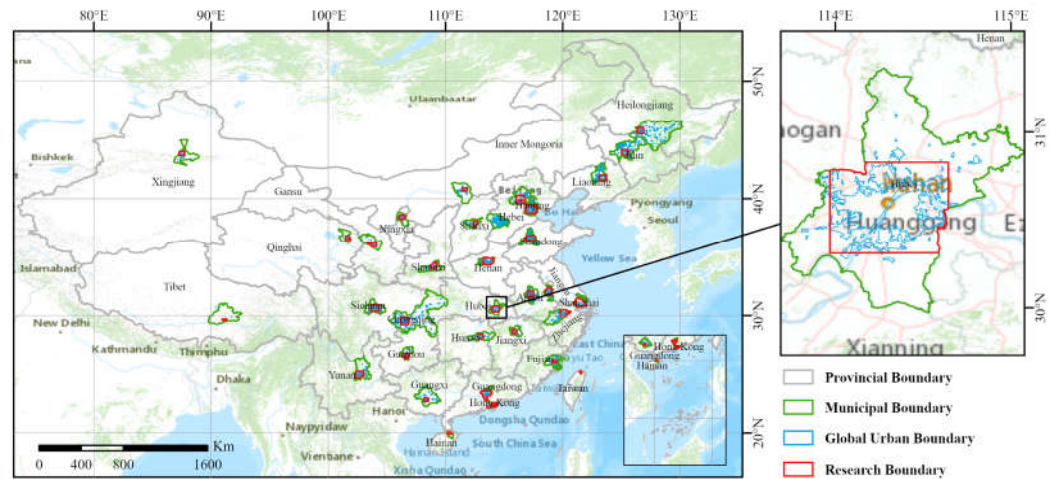


**Figure 2.** The geographic locations of the 34 Chinese cities. (Note: the gray line indicates the provincial boundary; the green line indicates the municipal boundary; the blue line indicates the global urban boundary; we take Wuhan city as an example to illustrate the determination of the research boundary, the red line.)

## 2.2. Datasets

In this study, we used Sentinel-2 surface reflectance data [51,52] for remote sensing image analysis and LCZ mapping. At present, Sentinel-2 is the highest resolution freely available satellite imagery, with spatial resolutions ranging from 10 to 60 m depending on the spectral band. Another benefit of Sentinel-2 data is that imagery is acquired of most locations on the Earth's surface every 5 days with two complementary satellites. Thus, these data are suitable for LCZ mapping. As previously mentioned, multi-seasonal remote sensing data is likely to improve LCZ mapping accuracy. Cloud cover, however, often obstructs the sensor's view of the ground in individual Sentinel-2 images. To mitigate cloud contamination effects, we generated seasonal mosaic images from the original Sentinel-2 images. The dates of multi-seasonal composite images used in this study are shown in Table S2 (136 seasonal composite images in total).

In addition to Sentinel-2 imagery, we also used additional geospatial datasets for analysis of the 34 urban areas. As mentioned previously, the GUB data and the administrative boundaries of cities are used to determine the research boundaries of each city. Population count data [53] was used (in combination with the LCZ maps we generated) to analyze the population distribution of each city at the intra-urban scale. The detailed methods for preprocessing Sentinel-2 and population data are presented in Section 2.3.1.

## 2.3. Methods

The flow chart of this study is shown in Figure 3. We first preprocessed sentinel-2 images for LCZ mapping and population counts for population distribution analysis in Section 2.3.1. The process of constructing the LCZ sample dataset for Chinese cities is described in Section 2.3.2. To achieve high-quality mapping of LCZ in 34 cities, a patch-based LCZ classification scheme (Scheme 1, S1) based on chessboard segmentation and multi-seasonal images is proposed in Section 2.3.3. To verify the effectiveness of our

scheme, the latest classification methodology (Scheme 2, S2) from the WUDAPT website was chosen for comparison, and the details are shown in Section 2.3.4. Finally, the analysis of population distribution based on LCZ types is carried out (Supplementary Materials Figure S1). The details are shown in Section 2.3.5.

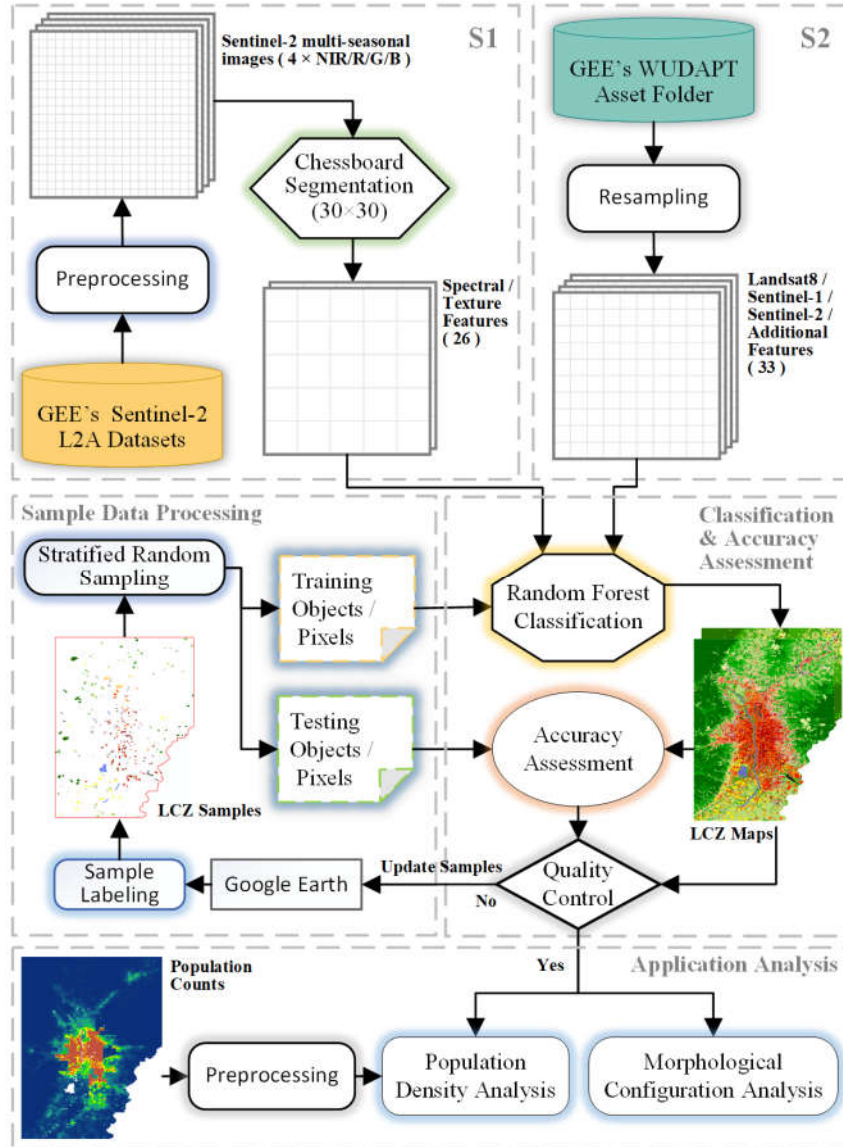


**Figure 3.** The workflow of LCZ classification method (S1 and S2), sample data processing, accuracy assessment, and application analysis.

### 2.3.1. Data Preprocessing

To obtain Sentinel-2 images of China’s provincial capital cities, Sentinel-2 L2A data was acquired using the Google Earth Engine web platform [54]. First, the Sentinel-2 L2A images were filtered by the regions of interest, dates, and cloud threshold to obtain the initial image datasets. The result of this was a dense stack of Sentinel-2 images having less than 10% cloud cover. Then, clouds remaining in these initial images were removed using the QA60 band of Sentinel-2, resulting in a set of cloud-filtered images. Finally, the cloud-filtered image dataset for each season was used to generate Sentinel-2 composite images by taking the median pixel value at each location (for each image band). As a result, a total

of 136 Sentinel-2 seasonal composite images were generated for the 34 cities, which were utilized for subsequent LCZ mapping.

To keep the resolution of population counts consistent with the results of LCZ mapping of Chinese cities, the population data are resampled to 300 m, and then, the pixel values are divided by the area represented by each grid. The population density data of Chinese cities with a resolution of 300 m are obtained for subsequent population distribution analysis.

### 2.3.2. LCZ Sample Dataset Construction

To solve the lack of LCZ samples in China, we manually collected training area data for the 34 provincial capital cities. First, following the definitions of each LCZ type [11], we digitized and labeled LCZ sample polygons by visual analysis of high-resolution images from Google Earth. In the process of sample labeling, we followed a few general criteria (<https://www.wudapt.org/digitize-training-areas>, accessed on 1 May 2022). Then, the initial mapping results were obtained using the random forest classifier based on the initial LCZ sample dataset and the Sentinel-2 seasonal composite imagery. Then, the classification maps were checked by us on Google Earth to ensure that the classification results were consistent with the ground truth. If there is an error, the boundary of sample polygons was modified, or additional sample polygons were added to facilitate classification again. The process of sample modification and classification needs to be repeated until the classification maps can accord with the actual condition. Finally, we have built a high-quality training sample set of LCZ in 34 Chinese cities. The number of LCZ sample polygons collected from each city is shown in Figure 4. Due to the difference in urban development level and urban landscape, the number of LCZ types varies from city to city.

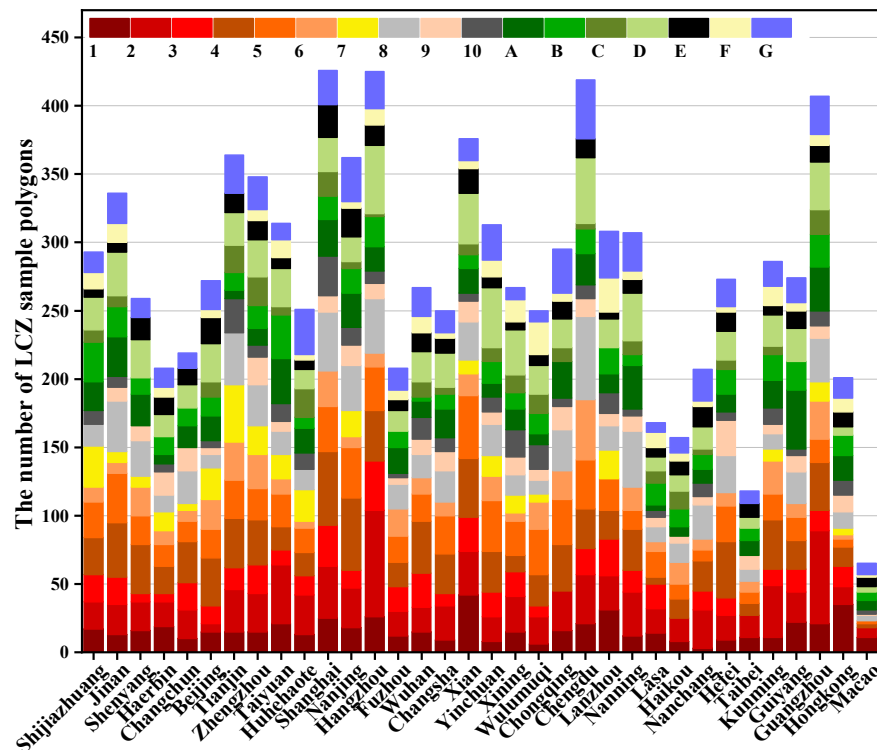


**Figure 4.** The number of sample polygons for different LCZ types in 34 Chinese cities.

### 2.3.3. LCZ Mapping Based on Chessboard Segmentation and Multi-Seasonal Images

To generate the LCZ maps of the 34 provincial capital cities of China, we proposed a patch-based LCZ classification framework (Scheme 1, S1) that uses chessboard segmentation and multi-seasonal images. Initially, to utilize the spatial and contextual information of neighboring pixels, the Sentinel-2 composite images were divided into patches of  $30 \times 30$  pixels in size through chessboard segmentation. Several patch-level spectral and texture features were then calculated. Patch-level spectral features include the average spectral value of each image band, maximum difference in pixel values for each image band, and brightness (i.e., average spectral values of all bands combined) for a total of 18 features. The texture features calculated included: homogeneity, contrast, dissimilarity, entropy, angular second moment, mean, standard deviation, and correlation calculated from the gray level co-occurrence matrix (GLCM), with eight features in total, as described in [55].

Next, the LCZ sample polygons obtained by manual sampling were used to label the segmentation patches, and the labeling criterion was set according to an overlap rate greater than 50%. To be consistent with the sampling rate of the latest WUDAPT method, 70% of the labeled patches were used as training samples, and 30% were used as validation samples. Here, a stratified random sampling strategy was used to obtain training samples and validation samples. The random forest classifier was chosen for LCZ mapping using these spectral/texture features because it is the state-of-the-art, non-parametric and efficient classifier, which is widely used in local climate zone classification tasks [26,29,56,57]. In keeping with the latest WUDAPT method, the classification process is repeated 25 times. We have also calculated several specialized accuracy metrics for LCZ mapping proposed in recent years, namely: overall accuracy (OA), the overall accuracy of urban LCZ types ( $OA_u$ ), the overall accuracy of built-up LCZ types ( $OA_{bu}$ ), and weighted accuracy ( $OA_w$ ). The specific definitions of these indexes can be found in [41,58].

#### 2.3.4. Latest WUDAPT Processing Method

To generate globally consistent LCZ maps more conveniently and quickly, Demuzere et al. [39] proposed a web application, LCZ Generator (Scheme 2, S2), which is based on the default WUDAPT classification workflow. LCZ Generator uses samples uploaded by researchers to carry out LCZ mapping and finally shares the corresponding LCZ classification maps on the website. Specifically, in addition to Landsat-8, other Earth observations are used, in combination with the LCZ samples, as input to the random forest classifier. A total of 33 features were used, including 16 features from Landsat-8, 5 features from Sentinel-1, 8 features from Sentinel-2, and 4 additional features, all of which have been resampled to a resolution of 100 m, as seen in detail [39]. To ensure the quality of the LCZ map, an automated cross-validation approach using 25 bootstraps is applied [41]. Then, 70% of the sample polygons in each bootstrap are used to train and 30% to test. The LCZ Generator outputs several LCZ map accuracy metrics, including OA,  $OA_u$ ,  $OA_{bu}$ , and  $OA_w$ .

#### 2.3.5. Population Distribution Analysis Based on LCZ Classification Results

Although the LCZ types are primarily a description of land cover, some of them can be linked to land use and population. The built LCZs have obvious features in building height, openness, and usage. Generally speaking, the higher and more compact the building is, the higher the population per unit area will be (assuming the buildings are mainly used for housing). As a result, the population density will theoretically vary between LCZs. To study the population distribution in LCZs in China, an overlay analysis of the LCZ results and population data was performed. In addition, the 32 cities (except for Macao and Lasa) in China are divided into four sizes, namely super city, megacity, type I large city, and type II large city according to the number of permanent residents. Then, the impact of city size on the population distribution in LCZ is analyzed.



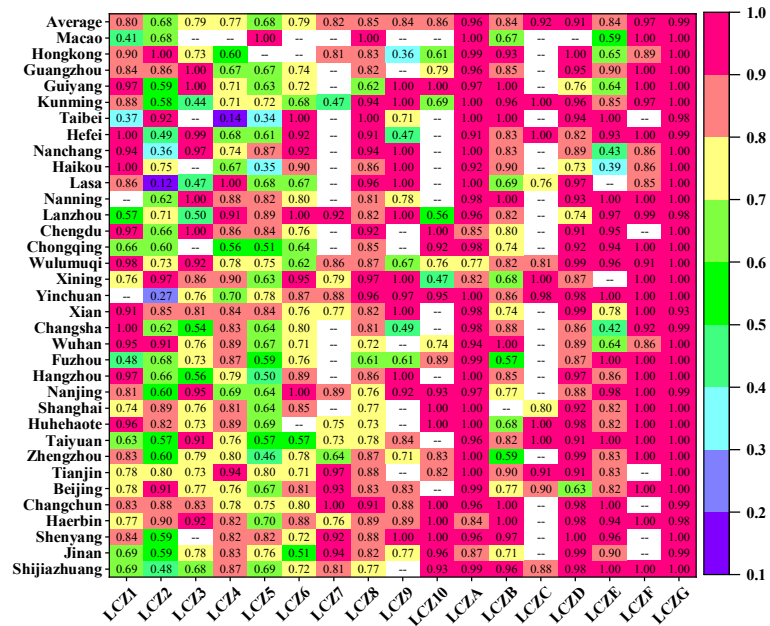


Figure 6. The accuracy of each LCZ type for the 34 cities and the average accuracy is given at the top line for all cities. Dashed lines indicate no accuracy score.

### 3.1.3. Accuracy Comparison between Our Method and WUDAPT

The LCZ training area samples with label information from 34 Chinese cities were uploaded to the WUDAPT website. Then, the mapping accuracy and results of LCZ for the corresponding cities were obtained after processing on the website platform. The mapping results are shown in Figure S1, and the relevant data can be found and downloaded at <https://lcz-generator.rub.de/>, accessed on 1 May 2022. To compare the LCZ classification accuracy of the two schemes, the four accuracy indicators of 34 cities under the two classification schemes were calculated and counted, as shown in Figure 7. Then, the four indicators of 34 cities were averaged to obtain Table 1.

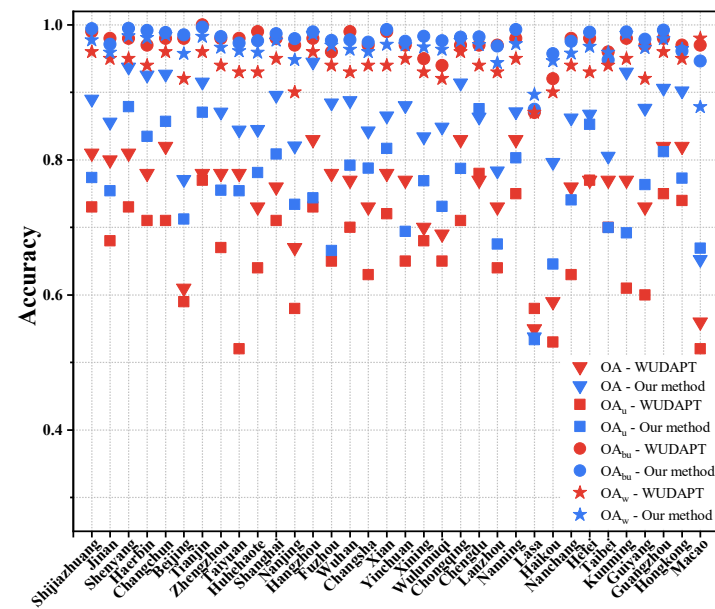


Figure 7. Comparison of four indicators ( $OA$ ,  $OA_u$ ,  $OA_{bu}$ , and  $OA_w$ ) under two schemes (our method, S1; WUDAPT method, S2) for the 34 cities.

**Table 1.** The average accuracy of four indicators under the two schemes.

Scheme	OA (%)	OA <sub>u</sub> (%)	OA <sub>bu</sub> (%)	OA <sub>w</sub> (%)
S1	85.45	75.99	97.66	96.33
S2	74.94	66.94	97.06	93.88

First, it can be seen from Figure 7 that the OA, OA<sub>u</sub>, OA<sub>bu</sub>, and OA<sub>w</sub> of 34 cities obtained by S1 are higher than those obtained by S2 in varying degrees. Second, it can be seen from Table 1 that the OA, OA<sub>u</sub>, OA<sub>bu</sub>, and OA<sub>w</sub> obtained by S1 are 85.45%, 75.99%, 97.66%, and 96.33%, respectively. The OA, OA<sub>u</sub>, OA<sub>bu</sub>, and OA<sub>w</sub> obtained by S2 are 74.94%, 66.94%, 97.06%, and 93.88%, respectively. The four indicators of S1 are 10.51%, 9.05%, 0.6%, and 2.45% higher than those of S2, indicating that the classification accuracy of S1 is better than that of S2 on the whole. The OA<sub>u</sub> of the two schemes is 8% and 9.46% less than that of OA, indicating that the classification accuracy of built types remains improved. Finally, more than 300 cities have uploaded LCZ samples to the WUDAPT website, and the average overall accuracy of LCZ mapping in all cities is 65.61%. By uploading LCZ samples from 34 Chinese cities to the WUDAPT website, the average overall accuracy of 34 cities is 74.94%, which meets the requirement of WUDAPT automatic quality control with an average minimum accuracy of 50% [41], indicating that the quality of LCZ samples constructed by us is high.

To more specifically compare the LCZ mapping results under different schemes, Fuzhou city is taken as an example to illustrate, as shown in Figure 8. First, on the whole, the LCZ classification result of S1 (our method) is more consistent with the remote sensing images in Google Earth than that of S2 (WUDAPT). In addition, it can be seen from regions 1 and 2 that there are many LCZ A misclassified into LCZ 9 under S2, and the classification results under S1 can more accurately describe the surface coverage. This is because the spectral information of some natural surface cover changes with seasons, and multi-seasonal images can introduce the phenological characteristics of vegetation to improve the accuracy of classification. Second, from the local point of view, it can be seen from region 3 and region 4 that the classification results of S2 can distinguish some smaller objects, such as LCZ A and LCZ G, but the classification results are more fragmented, and the classification effect is not as good as that of S1. Although S2 can describe the internal differences in urban morphology and surface characteristics in more detail, the noise is also larger and cannot represent homogeneous urban areas. In summary, the classification framework S1 was more robust, attained higher classification accuracy, and was easier to interpret (due to reducing the “salt-and-pepper” effect).

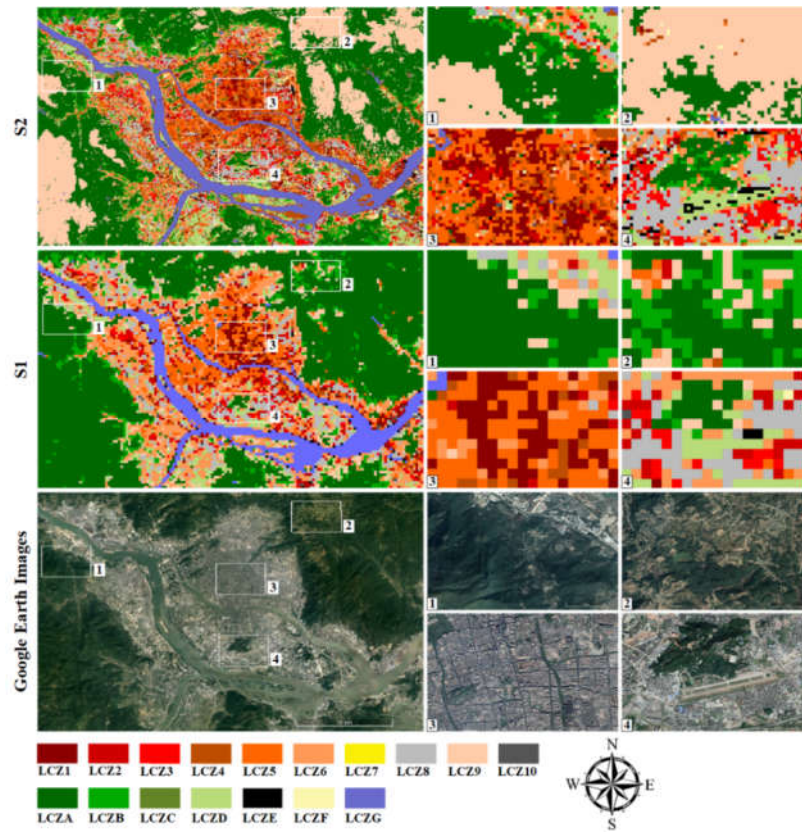


**Figure 8.** Comparison of LCZ mapping results under two schemes (S1 and S2): A case study of Fuzhou. The enlarged results of each scheme for the four subset areas (Box 1, 2, 3, and 4) are presented. Google Earth images of each region are also presented.

### 3.2. Relationship between LCZ TYPES and population

To obtain an overview of the 34 cities in China, the proportions of area and population for different built LCZ classes were counted, as shown in Figure 9. Among these classes, the large low-rise (LCZ 8) has the largest share of area, being 23.17% of the total built-up area and 14.43% of the total population. The sparsely built (LCZ 9) occupied 12.51% of the total built-up area, only accommodating 2.54% of the total population in 34 cities, and the lightweight low-rise (LCZ 7) held 6.11% of the total built-up area, accommodating 2.09% of the total population. Furthermore, 51.37% of the population lived in the open areas (LCZ 4–6), accounting for 41.62% of the total built-up area. However, the 13.26% compact area (LCZ 1–3) accommodated 26.74% of the total population. The difference in population density between compact high-rise (LCZ 1) and sparsely built (LCZ 9) was more than eighteen times.

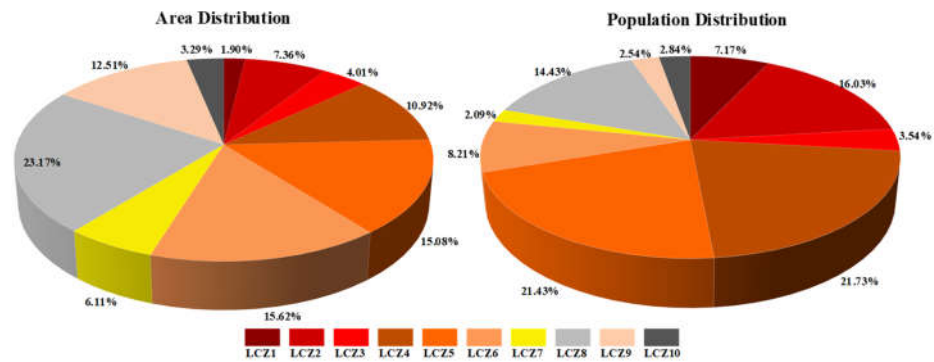


**Figure 9.** The proportions of area (left) and population (right) of the ten built-up classes (LCZ 1–10) for the 34 cities. A legend for the 3D colored pie chart is given at the bottom.

To further analyze the relationship between built-up LCZ types and population density, the heat map and histogram of population density (Figure 10a,b) at the LCZ scale were obtained by overlaying the LCZ results with population data. It can be seen from Figure 10a that LCZs 1–3 had the highest population density of 1372–83200 people/km<sup>2</sup>. LCZs 4–6 corresponded to a moderate level of population density, 384–21682 people/km<sup>2</sup>. LCZs 7–9 had the lowest population density of 0–5650 people/km<sup>2</sup>. Furthermore, there exists a decreasing trend of population density in LCZs 1–3 and LCZs 4–6, respectively. From Figure 10b, we found that the overall variation trend of population density in the built-up LCZ type was: LCZ 1 > LCZ 2 > LCZ 4 > LCZ 5 > LCZ 3 > LCZ 8 > LCZ 6 > LCZ 7 > LCZ 9. Among them, LCZ 1 had the highest population density of 19,222 people/km<sup>2</sup>, while LCZ 9 corresponded to the lowest population density of 1030 people/km<sup>2</sup>.

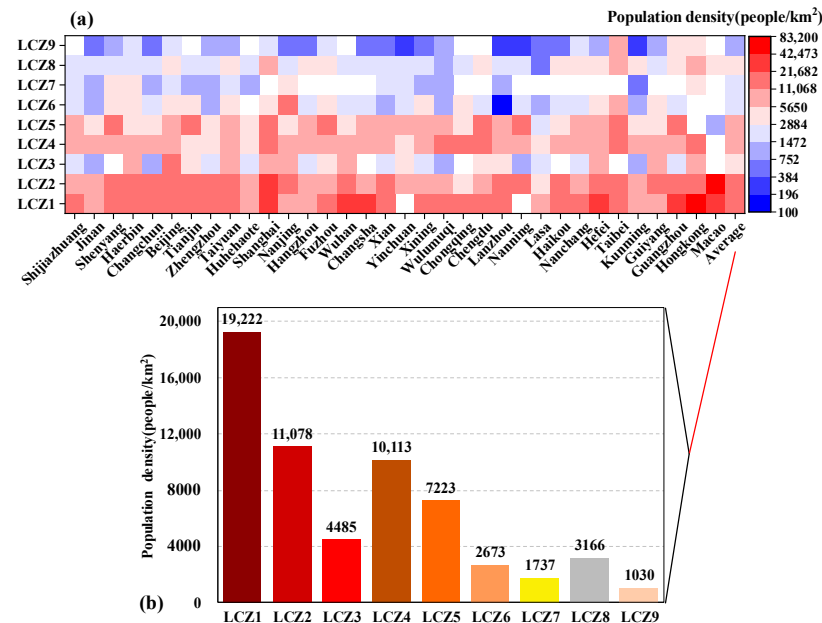


**Figure 10.** (a) Heat map of population density at the LCZ scale for 34 cities. (b) Histogram of average population density for each LCZ.

### 3.3. Population Density of LCZs in Different Size Cities

To further reveal the population distribution pattern of LCZs, the average population density of LCZs under different size cities was plotted. As shown in Figure 11, the hierarchical effect of population density in cities of different sizes was significant. In

relatively larger cities, the population density of all LCZs was high. The highest average population density was 7909 people/km<sup>2</sup> in super cities (1495 people/km<sup>2</sup> higher than that in megacities), 6414 people/km<sup>2</sup> in megacities (399 people/km<sup>2</sup> higher than that in type I large cities), and 6015 people/km<sup>2</sup> in type I large cities (864 people/km<sup>2</sup> higher than that in Type II large cities at 5151 people/km<sup>2</sup>). The difference in average population density between LCZs in megacities and type I large cities was the smallest, whereas that between LCZs in type II large cities and super cities was the largest. Consequently, there was a hierarchical effect of population density in LCZs of cities of different sizes in China in the following order: super cities > megacities > type I large cities > type II large cities. In addition, in the LCZ categories that had a relatively high population density, such as LCZ 1, LCZ 2, LCZ 3, LCZ 4, and LCZ 5, the difference in population density was relatively higher in different size cities, while in the LCZ categories that were with relatively low population density, such as LCZ 6, LCZ 7, and LCZ 9, the difference in population density was relatively lower in cities of different sizes.

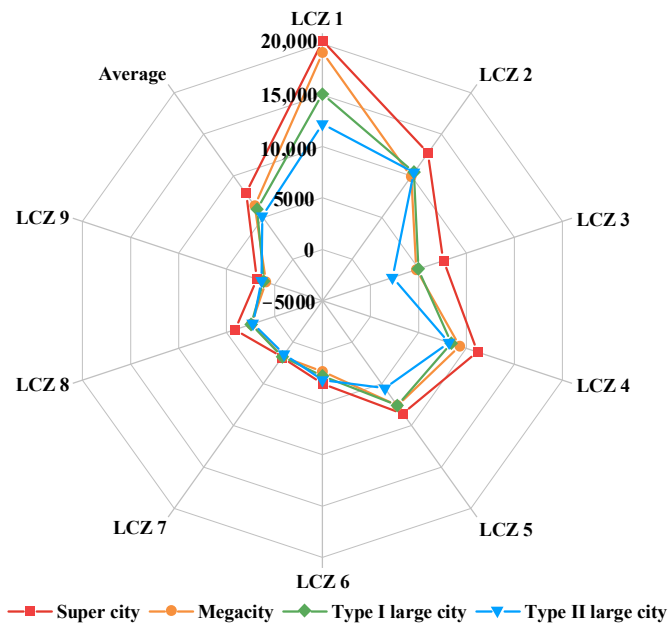


**Figure 11.** The radar chart of population density of LCZ types for different size cities. (Note: the red box represents supercity, the orange circle represents megacity, the green diamond represents type I large city, and the blue triangle represents type II large city.)

## 4. Discussion

### 4.1. Comparison with Traditional LCZ Classification Method

In the previous sections, we compared the proposed LCZ classification framework with the traditional method (S2) in terms of classification accuracy and visualization aspect. In this section, we further compare the two methods and present the limitations.

The built LCZ types often correspond to complex urban scenes containing many artificial structures with high spectral heterogeneity, and therefore, their classification accuracy is usually not high [41,42]. The results obtained by the S2 only through the pixel features of remote sensing images are not satisfactory, as the spatial information and phenological features are not fully utilized. However, our proposed method generates objects through chessboard segmentation and can make full use of spatial relationships and contextual information by calculating the texture features (GLCM) of the objects [36,61]. In addition, the stacked multi-seasonal images are used to exploit the phenological features carried by the surface objects. These steps are easily implemented by the software of eCognition [62]. In this way, the complex scenes consisting of multiple land-cover types

can be more effectively represented by adding neighborhood information and phenological characteristics.

The resolution adopted by the WUDAPT method is 100 m; however, this value may not be suitable for LCZ mapping. Considering the applicability of LCZ to climate research, Stewart and Oke [11] suggested that the minimum radius of each LCZ should be 200 to 500 m. By analyzing the correlation between LCZ and climatic parameters, Zheng et al. [28] found that the optimal resolution for LCZ classification in urban areas of Hong Kong is around 300 m. Research showed that neighborhood information had a positive influence on LCZ mapping [63], and the larger image size (320–640 m) was more suitable for LCZ mapping [44]. In addition, many scholars have adopted a resolution of around 300 m for LCZ mapping [36,64–66].

There still exist limitations to LCZ mapping based on remote sensing images. The accuracy of the built LCZ types is generally lower than that of the natural LCZ categories, as can be seen from Figure 6. The accuracy of LCZ A and LCZ G is generally high, which is due to the large distribution area and the difficulty to appear mixed ground objects. However, the accuracy of the classification of LCZs 1–6 is lower. This is due to the similarity of building materials in the same area and the lack of information on the 3D structure of buildings in the LCZ classification, making it difficult to distinguish between LCZs 1–3 or LCZs 4–6 only with a single data source of remote sensing imagery. Relevant urban data available at small scales, combined with the use of multiple sources (e.g., building morphology data, LiDAR data), will further improve the classification accuracy [24,42,67]. However, accurate and consistent data of height information at large scale scales (national or global) are still scarce. Even with these limitations, the accuracy of our proposed framework is still sufficient for subsequent population analysis.

#### *4.2. Application of LCZs in Combination with Population*

The built LCZ types inherently had distinct characteristics in building scale, height, density, and usage; thus, they will have different features in terms of population density. We analyzed the relationship between LCZs and population in 34 Chinese cities, and the results showed that the compact LCZs have a higher population density than open LCZs, with a maximum difference of 18 times (Figure 9). The huge differences in population density in LCZ reflected, to some extent, the inequalities in the living conditions of the Chinese people. Moreover, the compactness and height of the different LCZ classes were different, and thus, their population density was also different (Figure 10). Specifically, when comparing the population density of LCZs 1–3, we found that the higher the building is, the higher the population density of the corresponding LCZ type is. When comparing the population density in LCZs 1–3 and LCZs 4–6, we found that the more compact the building is, the higher the population density of the corresponding LCZ type is. The buildings are high and compact in LCZ 9, which has the highest population density. However, the buildings are low and sparse in LCZ 9, which has the lowest population density. In general, population density in built LCZs varies by type and is mainly affected by building height and density.

By analyzing the effect of different city sizes on population density in the LCZ, our results show that there was a hierarchical effect of population density in LCZs of cities of different sizes in China, in the following order: super cities > megacities > type I large cities > type II large cities (Figure 11). This is because the greater the scale of the city, the more people have; thus, the utilization efficiency of the land is higher. Furthermore, we found that the difference in population density between cities of different sizes is greater when in the LCZ class with higher population density. Since the height and density of the buildings in LCZ 6, 7, and 9 are low, the upper limit of the population density in these categories is not high; thus, the population density between different sizes of cities is small. Conversely, in the high-rise LCZ type (LCZ 1 and LCZ 4), the upper limit of building height is high, and larger cities tend to have more and taller buildings, which makes the difference in population density the largest.

#### 4.3. Possible Application Based on LCZ

LCZs were originally developed for metadata communication in temperature observation of a field site; thus, the urban heat island study is its main application [68]. Due to their detailed description of urban areas, a few studies have also applied the LCZ scheme to the studies of urban energy budgets [15], urban ventilation [17], and outdoor thermal comfort [20]. In recent years, the future land use simulation (FLUS) model was proposed by Liu et al. [69] and was successfully applied to the future spatial change simulation in the LCZ [70]. The urban morphological structure provided by LCZs is closely related to the transportation network, which is an important factor influencing the urban land use pattern, and its planning guides the direction of urban development [71]. By considering different transport planning policies, such as the sustainable urban mobility plan [72], we could simulate the spatial change pattern of the LCZ using the FLUS model for ex-ante assessment of the impact of transportation planning policies. Furthermore, by combining population data, the LCZ forecast results will provide credible data support for the adjustments of planning policy.

#### 5. Conclusions and Future Work

This study first constructed a high-quality training sample set with label information. Then, we proposed an LCZ classification framework based on chessboard segmentation and multi-seasonal Sentinel-2 images at a 300 m grid and used this framework to generate LCZ maps in 34 provincial capital cities of China. Subsequently, we evaluated the accuracy of the LCZ mapping results. In addition, we conducted an overlay analysis of the LCZ classification results and population density. The key findings of this study are summarized as follows:

(1) The values of overall accuracy in the 34 cities of China ranged from 75% to 94%, with an average of 85%. Compared with the latest WUDAPT method, the  $OA$ ,  $OA_u$ ,  $OA_{bu}$ , and  $OA_w$  values of our proposed framework increased by an average of 10%, 9%, 1%, and 2%, respectively. Meanwhile, the LCZ reference training sample set has been uploaded to the WUDAPT, which is available at <https://lcz-generator.rub.de/submissions>, accessed on 1 May 2022. Please cite the paper to use the dataset.

(2) The accuracy of different LCZ types varies. In general, the accuracy of natural LCZ types was higher than that of built LCZ types. The accuracy of the built LCZ type will be further improved by combining remote sensing images with multi-source data (e.g., building morphology data, LiDAR data, etc.) when relevant data are available.

(3) Population density in built LCZs varies by type and is mainly affected by building height and density. The overall variation trend of population density in the built-up LCZ type was: LCZ 1 > LCZ 2 > LCZ 4 > LCZ 5 > LCZ 3 > LCZ 8 > LCZ 6 > LCZ 7 > LCZ 9. Among them, the mean population density of LCZ 1 (compact high-rise) was highest (19,222 people/km<sup>2</sup>), whereas that of LCZ 9 (sparsely built) was lowest (1030 people/km<sup>2</sup>).

(4) There was a hierarchical effect of population density in LCZs of cities of different sizes in China in the following sequence: super cities > megacities > type I large cities > type II large cities. In addition, the difference in population density was higher in the LCZ types (LCZ 1, LCZ 2, LCZ 3, LCZ 4, and LCZ 5) that had relatively high population density, while the difference in population density was lower in the LCZ types (LCZ 6, LCZ 7, and LCZ 9) that had relatively low population density.

In conclusion, the high-quality LCZ training samples not only contribute to the production of LCZ maps at national or even global scales but also make sample transferability possible. Meanwhile, the proposed classification framework provided a valuable reference for improving the accuracy of LCZ mapping. Moreover, this study gave the population density in different built LCZs of Chinese cities and explored the influence of city size on it, which helps to understand population distribution patterns in China.

In the future, the Earth Engine (e.g., Google Earth Engine) with huge computing power will be used to map the whole of China into LCZ types with these high-quality

training sample. Furthermore, we intend to integrate multi-source data to improve the classification accuracy of LCZ, especially for built LCZ types. When the entire LCZ map of China is available, we could estimate the population of China by population density in LCZs of cities of different sizes in a low-cost way.

**Supplementary materials:** Comparison of LCZ classification results for 34 cities between the proposed method (Scheme 1) and the latest WUDAPT method (Scheme 2). Supplementary materials to this article can be found online at [www.mdpi.com/article/10.3390/ijgi11080420/s1](http://www.mdpi.com/article/10.3390/ijgi11080420/s1).

**Author Contributions:** Conceptualization, Liang Zhou and Lei Ma; Data curation, Liang Zhou; Formal analysis, Liang Zhou and Ziyun Yan; Funding acquisition, Lei Ma; Methodology, Liang Zhou and Lei Ma; Project administration, Lei Ma; Resources, Liang Zhou; Software, Lei Ma; Supervision, Lei Ma, Feixue Li, and Manchun Li; Validation, Lei Ma; Visualization, Liang Zhou; Writing—original draft, Liang Zhou; Writing—review and editing, Liang Zhou, Lei Ma, Brian Alan Johnson, and Ziyun Yan. All authors have read and agreed to the published version of the manuscript.

**Funding:** This research was funded by the National Natural Science Foundation of China (Grant Number: 42171304, 41701374) and the Fundamental Research Funds for the Central Universities.

**Institutional Review Board Statement:** Not applicable.

**Informed Consent Statement:** Not applicable.

**Data Availability Statement:** The LCZ sample dataset generated by this study can be found here: [<https://lcz-generator.rub.de/submissions>, accessed on 1 May 2022].

**Acknowledgments:** Sincere thanks to the anonymous reviewers and members of the editorial team for the comments and contributions.

**Conflicts of Interest:** The authors declare no conflict of interest.

## References

1. World Cities Report 2020: The Value of Sustainable Urbanization. Available online: [https://unhabitat.org/sites/default/files/2020/10/wcr\\_2020\\_report.pdf](https://unhabitat.org/sites/default/files/2020/10/wcr_2020_report.pdf) (accessed on 17 May 2022).
2. Kalnay, E.; Cai, M. Impact of urbanization and land-use change on climate. *Nature*. **2003**, *423*, 528–531.
3. Chen, X.; Zhao, H.; Li, P.; Yin, Z. Remote sensing image-based analysis of the relationship between urban heat island and land use/cover changes. *Remote Sens. Environ.* **2006**, *104*, 133–146.
4. Esch, T.; Marconcini, M.; Felbier, A.; Roth, A.; Heldens, W.; Huber, M.; Schwinger, M.; Taubenbock, H.; Muller, A.; Dech, S. Urban footprint processor—Fully automated processing chain generating settlement masks from global data of the TanDEM-X mission. *IEEE Geosci. Remote Sens. Lett.* **2013**, *10*, 1617–1621.
5. Pesaresi, M.; Huadong, G.; Blaes, X.; Ehrlich, D.; Ferri, S.; Gueguen, L.; Halkia, M.; Kauffmann, M.; Kemper, T.; Lu, L.; et al. A global human settlement layer from optical HR/VHR RS data: concept and first results. *IEEE J. Sel. Top. Appl. Earth Observ. Remote Sens.* **2013**, *6*, 2102–2131.
6. Gong, P.; Li, X.; Wang, J.; Bai, Y.; Chen, B.; Hu, T.; Liu, X.; Xu, B.; Yang, J.; Zhang, W.; et al. Annual maps of global artificial impervious area (GAIA) between 1985 and 2018. *Remote Sens. Environ.* **2020**, *236*, 111510.
7. Chen, J.; Chen, J.; Liao, A.; Cao, X.; Chen, L.; Chen, X.; He, C.; Han, G.; Peng, S.; Lu, M.; et al. Global land cover mapping at 30m resolution: a POK-based operational approach. *ISPRS J. Photogramm. Remote Sens.* **2015**, *103*, 7–27.
8. Gong, P.; Liu, H.; Zhang, M.; Li, C.; Wang, J.; Huang, H.; Clinton, N.; Ji, L.; Li, W.; Bai, Y.; et al. Stable classification with limited sample: transferring a 30-m resolution sample set collected in 2015 to mapping 10-m resolution global land cover in 2017. *Sci. Bull.* **2019**, *64*, 370–373.
9. Bontemps, S.; Boettcher, M.; Brockmann, C.; Kirches, G.; Lamarche, C.; Radoux, J.; Santoro, M.; Vanbogaert, E.; Wegmüller, U.; Herold, M.; et al. Multi-year global land cover mapping at 300 m and characterization for climate modelling: achievements of

- the land cover component of the ESA climate change initiative. In Proceedings of the 2015 36th International Symposium on Remote Sensing of Environment, Berlin, Germany, 11–15 May 2015; pp. 323–328.
10. Zhu, X.X.; Qiu, C.; Hu, J.; Shi, Y.; Wang, Y.; Schmitt, M.; Taubenböck, H. The urban morphology on our planet – Global perspectives from space. *Remote Sens. Environ.* **2022**, *269*, 112794.
  11. Stewart, I.; Oke, T.R. Local climate zone for urban temperature studies. *B. Am. Meteorol. Soc.* **2012**, *93*, 1879–1900.
  12. Jiang, S.; Zhan, W.; Yang, J.; Liu, Z.; Huang, F.; Lai, M.; Li, J.; Hong, F.; Huang, Y.; Chen, J.; et al. Urban heat island studies based on local climate zones: A systematic overview. *Acta Geogr. Sin.* **2020**, *75*, 1860–1878.
  13. Perera, N.G.R.; Emmanuel, R. A “local climate zone” based approach to urban planning in Colombo, Sri Lanka. *Urban Clim.* **2018**, *23*, 188–203.
  14. Pradhesta, Y.F.; Nurjani, E.; Arijuddin, B.I. Local climate zone classification for climate-based urban planning using landsat 8 imagery (a case study in Yogyakarta urban area). *IOP Conf. Ser.: Earth Environ. Sci.* **2019**, *303*, 12022.
  15. Alexander, P.J.; Mills, G.; Fealy, R. Using LCZ data to run an urban energy balance model. *Urban Clim.* **2015**, *13*, 14–37.
  16. Quan, S.J.; Dutt, F.; Woodworth, E.; Yamagata, Y.; Yang, P.P. Local climate zone mapping for energy resilience: a fine-grained and 3D approach. *Energy Procedia.* **2017**, *105*, 3777–3783.
  17. Yang, J.; Jin, S.; Xiao, X.; Jin, C.; Xia, J.C.; Li, X.; Wang, S. Local climate zone ventilation and urban land surface temperatures: towards a performance-based and wind-sensitive planning proposal in megacities. *Sustain. Cities Soc.* **2019**, *47*, 101487.
  18. Zhao, Z.; Shen, L.; Li, L.; Wang, H.; He, B. Local climate zone classification scheme can also indicate local-scale urban ventilation performance: an evidence-based study. *Atmosphere-Basel.* **2020**, *11*, 776.
  19. Zhang, Y.; Zhang, X.; Xu, W.; Jiao, B. A case study on urban ventilation assessment with local climate zone (LCZ) parameters. *IOP Conf. Ser.: Earth Environ. Sci.* **2021**, *696*, 012033.
  20. Kotharkar, R.; Bagade, A.; Agrawal, A. Investigating local climate zones for outdoor thermal comfort assessment in an Indian city. *Geogr. Pannonica.* **2019**, *23*, 318–328.
  21. Lau, K.K.; Chung, S.C.; Ren, C. Outdoor thermal comfort in different urban settings of sub-tropical high-density cities: an approach of adopting local climate zone (LCZ) classification. *Build. Environ.* **2019**, *154*, 227–238.
  22. Stewart, I.D.; Oke, T.R.; Krayerhoff, E.S. Evaluation of the ‘local climate zone’ scheme using temperature observations and model simulations. *Int. J. Climatol.* **2014**, *34*, 1062–1080.
  23. Demuzere, M.; Hankey, S.; Mills, G.; Zhang, W.; Lu, T.; Bechtel, B. Combining expert and crowd-sourced training data to map urban form and functions for the continental US. *Sci. Data.* **2020**, *7*, 1–13.
  24. Hu, J.; Wang, Y.; Taubenböck, H.; Zhu, X.X. Land consumption in cities: a comparative study across the globe. *Cities.* **2021**, *113*, 103163.
  25. Lelovics, E.; Unger, J.; Gál, T.; Gál, C.V. Design of an urban monitoring network based on local climate zone mapping and temperature pattern modelling. *Clim. Res.* **2014**, *60*, 51–62.
  26. Bechtel, B.; Alexander, P.; Böhner, J.; Ching, J.; Conrad, O.; Feddema, J.; Mills, G.; See, L.; Stewart, I. Mapping local climate zones for a worldwide database of the form and function of cities. *ISPRS Int. J. Geo-Inf.* **2015**, *4*, 199–219.
  27. Aman, A.; Khan, M.M.; Khurshid, K. Comparative analysis of different methodologies for local climate zone classification. *Sci. Int.* **2018**, *30*, 925–934.
  28. Zheng, Y.; Ren, C.; Xu, Y.; Wang, R.; Ho, J.; Lau, K.; Ng, E. GIS-based mapping of local climate zone in the high-density city of Hong Kong. *Urban Clim.* **2018**, *24*, 419–448.
  29. Demuzere, M.; Bechtel, B.; Mills, G. Global transferability of local climate zone models. *Urban Clim.* **2019**, *27*, 46–63.
  30. Quan, S.J.; Bansal, P. A systematic review of GIS-based local climate zone mapping studies. *Build. Environ.* **2021**, *196*, 107791.
  31. Bechtel, B.; Daneke, C. Classification of local climate zones based on multiple earth observation data. *IEEE J. Sel. Top. Appl. Earth Observ. Remote Sens.* **2012**, *5*, 1191–1202.

32. Xu, Y.; Ren, C.; Cai, M.; Edward, N.Y.Y.; Wu, T. Classification of local climate zones using aster and landsat data for high-density cities. *IEEE J. Sel. Top. Appl. Earth Observ. Remote Sens.* **2017**, *10*, 3397-3405.
33. Hu, J.; Ghamisi, P.; Zhu, X. Feature extraction and selection of sentinel-1 dual-pol data for global-scale local climate zone classification. *ISPRS Int. J. Geo-Inf.* **2018**, *7*, 379.
34. Yoo, C.; Han, D.; Im, J.; Bechtel, B. Comparison between convolutional neural networks and random forest for local climate zone classification in mega urban areas using landsat images. *ISPRS J. Photogramm. Remote Sens.* **2019**, *157*, 155-170.
35. Chen, T.K.; Qiu, C.; Schmitt, M.; Zhu, X.X.; Sabel, C.E.; Prishchepov, A.V. Mapping horizontal and vertical urban densification in Denmark with landsat time-series from 1985 to 2018: a semantic segmentation solution. *Remote Sens. Environ.* **2020**, *251*, 112096.
36. Huang, X.; Liu, A.; Li, J. Mapping and analyzing the local climate zones in China's 32 major cities using landsat imagery based on a novel convolutional neural network. *Geo. Spat. Inf. Sci.* **2021**, *24*, 528-557.
37. Breiman, L. Random forests. *Mach. Learn.* **2021**, *45*, 5-32.
38. Ching, J.; Mills, G.; Bechtel, B.; See, L.; Feddema, J.; Wang, X.; Ren, C.; Brousse, O.; Martilli, A.; Neophytou, M.; et al. WUDAPT: an urban weather, climate, and environmental modeling infrastructure for the anthropocene. *B. Am. Meteorol. Soc.* **2018**, *99*, 1907-1928.
39. Demuzere, M.; Kittner, J.; Bechtel, B. LCZ generator: a web application to create local climate zone maps. *Front. Environ. Sci.* **2021**, *9*, 1-18.
40. Demuzere, M.; Bechtel, B.; Middel, A.; Mills, G. Mapping Europe into local climate zones. *PLoS One.* **2019**, *14*, e214474.
41. Bechtel, B.; Alexander, P.J.; Beck, C.; Böhner, J.; Brousse, O.; Ching, J.; Demuzere, M.; Fonte, C.; Gál, T.; Hidalgo, J.; et al. Generating WUDAPT level 0 data – current status of production and evaluation. *Urban Clim.* **2019**, *27*, 24-45.
42. Ren, C.; Cai, M.; Li, X.; Zhang, L.; Wang, R.; Xu, Y.; Ng, E. Assessment of local climate zone classification maps of cities in china and feasible refinements. *Sci. Rep.* **2019**, *9*.
43. Risojevic, V.; Babic, Z. Fusion of global and local descriptors for remote sensing image classification. *IEEE Geosci. Remote Sens. Lett.* **2013**, *10*, 836-840.
44. Liu, S.; Shi, Q. Local climate zone mapping as remote sensing scene classification using deep learning: a case study of metropolitan china. *ISPRS J. Photogramm. Remote Sens.* **2020**, *164*, 229-242.
45. Yoo, C.; Lee, Y.; Cho, D.; Im, J.; Han, D. Improving local climate zone classification using incomplete building data and sentinel 2 images based on convolutional neural networks. *Remote Sens.-Basel.* **2020**, *12*, 3552.
46. Zhu, X.; Liu, D. Accurate mapping of forest types using dense seasonal landsat time-series. *ISPRS J. Photogramm. Remote Sens.* **2014**, *96*, 1-11.
47. Zhao, Y.; Feng, D.; Yu, L.; Wang, X.; Chen, Y.; Bai, Y.; Hernández, H.J.; Galleguillos, M.; Estades, C.; Biging, G.S.; et al. Detailed dynamic land cover mapping of Chile: accuracy improvement by integrating multi-temporal data. *Remote Sens. Environ.* **2016**, *183*, 170-185.
48. Qiu, C.; Mou, L.; Schmitt, M.; Zhu, X.X. Local climate zone-based urban land cover classification from multi-seasonal sentinel-2 images with a recurrent residual network. *ISPRS J. Photogramm. Remote Sens.* **2019**, *154*, 151-162.
49. Shi, L.; Ling, F. Local climate zone mapping using multi-source free available datasets on google earth engine platform. *Land.* **2021**, *10*, 454.
50. Notice of the state council on adjusting the standards for the classification of cities. Available online: [http://www.gov.cn/zhengce/content/2014-11/20/content\\_9225.htm](http://www.gov.cn/zhengce/content/2014-11/20/content_9225.htm) (accessed on 17 May 2022).
51. Berger, M.; Moreno, J.; Johannessen, J.A.; Levelt, P.F.; Hanssen, R.F. ESA's sentinel missions in support of earth system science. *Remote Sens. Environ.* **2012**, *120*, 84-90.
52. Drusch, M.; Del Bello, U.; Carlier, S.; Colin, O.; Fernandez, V.; Gascon, F.; Hoersch, B.; Isola, C.; Laberinti, P.; Martimort, P.; et al. Sentinel-2: ESA's optical high-resolution mission for GMES operational services. *Remote Sens. Environ.* **2012**, *120*, 25-36.

53. Tatem, A.J. Worldpop, open data for spatial demography. *Sci. Data*. **2017**, *4*.
54. Gorelick, N.; Hancher, M.; Dixon, M.; Ilyushchenko, S.; Thau, D.; Moore, R. Google earth engine: planetary-scale geospatial analysis for everyone. *Remote Sens. Environ.* **2017**, *202*, 18-27.
55. Laliberte, A.S.; Rango, A. Texture and scale in object-based analysis of subdecimeter resolution unmanned aerial vehicle (UAV) imagery. *IEEE T. Geosci. Remote.* **2009**, *47*, 761-770.
56. Tuia, D.; Moser, G.; Le Saux, B.; Bechtel, B.; See, L. 2017 IEEE GRSS data fusion contest: open data for global multimodal land use classification. *IEEE Geosc. Rem. Sen. M.* **2017**, *5*, 70-73.
57. Ma, L.; Zhu, X.; Qiu, C.; Blaschke, T.; Li, M. Advances of local climate zone mapping and its practice using object-based image analysis. *Atmosphere-Basel*. **2021**, *12*, 1146.
58. Bechtel, B.; Demuzere, M.; Sismanidis, P.; Fenner, D.; Brousse, O.; Beck, C.; Van Coillie, F.; Conrad, O.; Keramitsoglou, I.; Middel, A.; et al. Quality of crowdsourced data on urban morphology—the human influence experiment (HUMINEX). *Urban Sci.* **2017**, *1*, 15.
59. Millard, K.; Richardson, M. On the importance of training data sample selection in random forest image classification: a case study in peatland ecosystem mapping. *Remote Sens-Basel*. **2015**, *7*, 8489-8515.
60. Belgiu, M.; Csillik, O. Sentinel-2 cropland mapping using pixel-based and object-based time-weighted dynamic time warping analysis. *Remote Sens. Environ.* **2018**, *204*, 509-523.
61. Kuffer, M.; Pfeffer, K.; Sliuzas, R.; Baud, I. Extraction of slum areas from VHR imagery using GLCM variance. *IEEE J. Sel. Top. Appl. Earth Observ. Remote Sens.* **2016**, *9*, 1830-1840.
62. Drăguț, L.; Csillik, O.; Eisank, C.; Tiede, D. Automated parameterisation for multi-scale image segmentation on multiple layers. *ISPRS J. Photogramm. Remote Sens.* **2014**, *88*, 119-127.
63. Verdonck, M.; Okujeni, A.; van der Linden, S.; Demuzere, M.; De Wulf, R.; Van Coillie, F. Influence of neighbourhood information on 'local climate zone' mapping in heterogeneous cities. *Int. J. Appl. Earth Obs.* **2017**, *62*, 102-113.
64. Zhao, C.; Jensen, J.L.R.; Weng, Q.; Currit, N.; Weaver, R. Use of local climate zones to investigate surface urban heat islands in Texas. *Glsci. Remote Sens.* **2020**, *57*, 1083-1101.
65. Zhou, Y.; Zhang, G.; Jiang, L.; Chen, X.; Xie, T.; Wei, Y.; Xu, L.; Pan, Z.; An, P.; Lun, F. Mapping local climate zones and their associated heat risk issues in Beijing: based on open data. *Sustain. Cities Soc.* **2021**, *74*, 103174.
66. Zhao, C.; Weng, Q.; Wang, Y.; Hu, Z.; Wu, C. Use of local climate zones to assess the spatiotemporal variations of urban vegetation phenology in Austin, Texas, USA. *Glsci. Remote Sens.* **2022**, *59*, 393-409.
67. Zhao, C.; Weng, Q.; Hersperger, A.M. Characterizing the 3-D urban morphology transformation to understand urban-form dynamics: a case study of Austin, Texas, USA. *Landsc. Urban Plan.* **2020**, *203*, 103881.
68. Xue, J.; You, R.; Liu, W.; Chen, C.; Lai, D. Applications of Local Climate Zone Classification Scheme to Improve Urban Sustainability: A Bibliometric Review. *Sustain.* **2020**, *12*, 8083.
69. Liu, X.; Liang, X.; Li, X.; Xu, X.; Qu, J.; Chen, Y.; Li, S.; Wang, S.; Pei, F. A future land use simulation model (FLUS) for simulating multiple land use scenarios by coupling human and natural effects. *Landsc. Urban Plan.* **2017**, *168*, 94-116.
70. Chen, G.; Xie, J.; Li, W.; Li, X.; Chung, L.C.H.; Ren, C.; Liu, X. Future "local climate zone" spatial change simulation in Greater Bay Area under the shared socioeconomic pathways and ecological control line. *Build. Environ.* **2021**, *203*, 108077.
71. Liang, X.; Liu, X.; Li, D.; Zhao, H.; Chen, G. Urban growth simulation by incorporating planning policies into a CA-based future land-use simulation model. *Int. J. Geogr. Inf. Sci.* **2018**, *32*(11), 2294-2316.
72. Russo, F.; Rindone, C. Regional Transport Plans: From Direction Role Denied to Common Rules Identified. *Sustain.* **2021**, *13*, 9052.